Ultramicroscopy 281 (2026) 114295

Contents lists available at ScienceDirect

Ultramicroscopy

journal homepage: www.elsevier.com/locate/ultramic

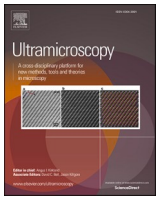

Validating electron pair distribution function analysis: The role of multiple scattering, beam, measurement, and processing parameters

Sangjun Kang [b,c,d,1,*], Hyeyoung Cho [b,c,1], Maximilian Töllner [b,c], Vanessa Wollersen [c], Di Wang [c,d], Hionsuck Baik [e], Marie Joëlle Perera [f], Omar Adjaoud [f], Karsten Albe [f], Christian Kübel [b,c,d,*], Xiaoke Mu [a,c,*]

[a] School of Materials and Energy and Electron Microscopy Centre, Lanzhou University, Lanzhou 730000, China
[b] In situ Electron Microscopy, Department of Materials Science, Technical University of Darmstadt (TUDa), 64287 Darmstadt, Germany
[c] Institute of Nanotechnology (INT), Karlsruhe Institute of Technology (KIT), 76344 Eggenstein-Leopoldshafen, Germany
[d] Karlsruhe Nano Micro Facility (KNMFi), Karlsruhe Institute of Technology (KIT), 76344 Eggenstein-Leopoldshafen, Germany
[e] Korea Basic Science Institute (KBSI), 34133 Daejeon, Korea
[f] Technische Universität Darmstadt, Fachbereich Material- und Geowissenschaften, Fachgebiet Materialmodellierung, Otto-Berndt-Str. 3, D-64287 Darmstadt, Germany

ARTICLE INFO

Keywords:
Electron pair distribution function
Radial distribution function
Four-dimensional scanning transmission electron microscopy
STEM-PDF

ABSTRACT

Electron pair distribution function (ePDF), combined with four-dimensional scanning transmission electron microscopy (4D-STEM), provides a powerful approach for uncovering detailed information about the local atomic structure and structural variations in disordered materials. However, achieving high accuracy in ePDF analysis requires careful control of experimental and instrumental parameters. In this study, we systematically investigate the effect of key electron optical, measurement and processing parameters on ePDF analysis using simulations as the primary tool, complemented by experimental validation. Specifically, we examine the influence of diffraction angle range, beam convergence semi-angle, detector pixel resolution, sample thickness (multiple scattering effect), noise, and electron beam precession on the resulting ePDF. By integrating multi-slice electron diffraction simulations with experimental diffraction data, we identify optimal conditions for accurate ePDF extraction and provide practical guidelines to improve analysis precision and reliability. These insights contribute to refining ePDF techniques, particularly for applications involving amorphous and nanostructured materials.

1. Introduction

Atomic pair distribution function (PDF) analysis provides real-space information on the atomic structure of materials by measuring the relative atomic density as a function of interatomic distance [1–11]. It is particularly useful for amorphous and nanostructured materials, where the inherent disorder in the structure renders direct microscopic imaging and traditional diffraction techniques challenging. Conventionally, PDFs are obtained via X-ray or neutron scattering to probe bulk structures, but the limited spatial resolution of these methods prevents investigation of local structural heterogeneities in glasses [5–7,10]. In contrast, electron microscopy-based methods, particularly scanning transmission electron microscopy (STEM), can focus the electron source to nanometer-scale volumes, e.g. nanobeam electron diffraction (NBED), enabling PDF analysis from localized nano-regions [3,12–15].

The development of 4D-STEM has significantly advanced the application of local ePDF analysis. 4D-STEM records 2D local diffraction patterns at every probe position on a stepwise scanned 2D grid of the probe over an extensive area of interest [16]. This technique results in a comprehensive 4D dataset that integrates both spatial and diffraction information. Within this 4D-STEM framework, fluctuation electron microscopy (FEM) and angular correlation analysis exemplify analysis modes that exploit spatially resolved diffraction to probe nanoscale ordering and orientational correlations [17–19]. Building on the same data structure, 4D-STEM further enables ePDF extraction while also combining ePDFs with imaging capability, providing simultaneous structural and spatial information [20–26]. However, achieving high accuracy in ePDF analysis is nontrivial. Various factors related to

* Corresponding authors.
E-mail addresses: sangjun.kang@tu-darmstadt.de (S. Kang), christian.kuebel@kit.edu (C. Kübel), muxk@lzu.edu.cn (X. Mu).
[1] Sangjun Kang and Hyeyoung Cho contributed equally to this work

https://doi.org/10.1016/j.ultramic.2025.114295
Received 30 June 2025; Received in revised form 6 November 2025; Accepted 6 December 2025
Available online 7 December 2025

electron optics, detector, and sample condition can significantly influence the quality and accuracy of the obtained PDF and complicate its quantitative interpretation [14,27–29]. In particular, multiple scattering, noise, limited detector size and resolution, and differences of the illumination conditions (e.g., beam convergence) are known to affect the diffraction data and thus the derived ePDF. More specifically, multiple scattering within the sample in thicker specimens contributes to an increased diffraction background with structured artifacts that complicate the interpretation of spatial frequency information [28]. To partially mitigate the effects, as well as inelastic scattering contributions, a smooth polynomial background subtraction is typically applied for ePDF calculations [20,23,25,26]. Moreover, detector attributes, such as dynamic range and pixel sampling, can limit the measurable intensity and angular range, and the probe convergence angle controls the angular resolution of diffraction features. Understanding the interplay of these factors is essential for optimizing experiments and obtaining reliable ePDFs. However, a comprehensive study that systematically evaluates these key parameters is lacking.

In this work, we address this gap by systematically investigating the effects of electron optics, detector, and sample conditions on ePDF determination. As model systems, we conducted molecular dynamics (MD) simulations to create a representative atomic model for a $Pd_{80}Si_{20}$ metallic glass. We conducted multislice electron diffraction simulations based on this atomic model to systematically vary measurement parameters and assess their effects on the resulting ePDF, and compared it with the ePDF from pure kinematic electron diffraction and the PDF directly counted from the original atomic model. We then perform selected area electron diffraction (SAED) and nano-beam electron diffraction (NBED) experiments on melt-quenched $Pd_{80}Si_{20}$ and $Fe_{85.2}Si_{0.5}B_{9.5}P_4Cu_{0.8}$ metallic glasses to validate the simulation predictions under practical conditions. As a step towards the generalization of the observations, detailed experimental analyses have been performed for a more complex Fe-based metallic glass sample with varying experimental parameters. Through this combined approach, we establish optimal conditions for quantitative ePDF analysis and provide guidelines for the experimental setup. By improving the reliability and accuracy of ePDF measurements, these results help to refine electron diffraction techniques for local structure characterization in disordered materials and glasses.

2. Methods

2.1. Atomic structure simulations

MD simulations have been used to generate realistic atomic structures for amorphous alloys. A model $Pd_{80}Si_{20}$ (at. %) metallic glass was prepared using the LAMMPS MD package [30] with an embedded-atom method (EAM) potential developed by Ding et al. for Pd–Si [31]. This potential accurately reproduces the structure of liquid and amorphous Pd–Si and has been validated in previous studies [32–34]. The simulation cell, representing a metallic glass, contains 399,469 atoms within a cubic volume of 179.989 × 179.989 × 179.989 Å^3. The melt was equilibrated at 2000 K for 2 ns and then quenched to 50 K at 0.01 K/ps to produce an amorphous structure. Temperature and pressure were controlled using a Nosé–Hoover thermostat and barostat, as implemented in LAMMPS [30]. This produced a well-relaxed atomic configuration representative of a $Pd_{80}Si_{20}$ metallic glass.

2.2. Electron diffraction simulations

Electron diffraction patterns were simulated for the above atomic models using the multi-slice method implemented in abTEM [35]. Multislice-based electron diffraction simulations were performed using a pixelated detector configuration in abTEM for NBED data acquisition [35], with the following parameters: an accelerating voltage of 300 kV, zero defocus, a slice thickness of 2 Å, 30 × 30 scan positions with a step size of 3.33 Å, and a single frozen phonon (FP) configuration with atomic displacements following a Gaussian distribution with a standard deviation of σ = 0.1 Å, and a potential based on the Independent Atom Model (IAM) using the Lobato and Van Dyck parametrization with infinite projection [36]. To verify the adequacy of using a single FP configuration, we compared simulations averaged for multiple FP configurations (up to 10). The resulting *S(k)* and PDF showed negligible differences (Figure S1), confirming that the substantial static disorder in the metallic glass model sufficiently represents the random displacements otherwise introduce through many FP configurations, thus properly reflecting the observed diffraction signal.

Simulated NBED diffraction patterns from multiple probe positions were averaged to improve the signal of sampling statistics and were subsequently used for ePDF analysis. To systematically investigate the influence of key experimental parameters on ePDF analysis, multiple simulation series were conducted. To investigate the influence of sample thickness, simulations were performed by extracting exit-plane data corresponding to thicknesses ranging from 200 Å to 1000 Å. The influence of convergence semi-angle was investigated through simulations with values ranging from 0 mrad (SADP condition) to 1.5 mrad; the corresponding probe diameters at full width at half maximum were 32.87 Å, 16.70 Å, 11.07 Å, 8.26 Å, and 6.86 Å at 0.3, 0.6, 0.9, 1.2, and 1.5 mrad, respectively. Additionally, precession NBED simulations were performed with a precession angle of 1° and 3° To investigate noise effects, Poisson noise corresponding to 10 e^- and 100 e^- per diffraction pattern at each scan position was applied using a fixed random seed of 100 and compared with diffraction simulations at infinite electron dose. These dose levels represent 9000 e^- and 90,000 e^- total electrons per diffraction pattern.

Detector pixel size, noise, and electron beam precession are critical aspects in 4D-STEM experiments, as the large data volume and long acquisition time can complicate data analysis and limit experimental efficiency. Therefore, these parameters were analyzed under NBED converging beam conditions to mimic a typical 4D-STEM experiment. In contrast, parameters including sample thickness, multiple scattering, *k* range, and the use of a beam stop were examined under parallel beam conditions (SAED), which provide higher signal-to-noise ratios and better angular resolution.

To benchmark the multiple scattering results and mimic the ideal "thin-sample" condition, we performed kinematic simulations using the Debye scattering equation [37,38], in which the scattered intensity is given by:

$$I_{kin}(k) = \sum_{i,j} f_i(k) f_j(k) \frac{\sin(kr_{ij})}{kr_{ij}},$$

Where r_{ij} is the interatomic distance between atoms i and j, and $f_i(k)$ and $f_j(k)$ are the atomic form factors. These simulations, which assume purely kinematic, single-scattering behavior, allowed us to isolate intrinsic structural contributions to *S(k)* without dynamical effects, thereby providing a reference to assess the influence of sample thickness and multiple scattering.

2.3. Sample preparation

A $Pd_{80}Si_{20}$ (at. %) metallic glass ribbon, approximately 25 mm in width and ~20 μm in thickness, was fabricated via melt spinning onto a copper wheel. Thin lamellae for TEM were prepared using focused ion beam (FIB) milling (FEI Strata 400S). Final thinning was performed to achieve ~50 nm thickness at the area of interest for electron transparency, employing a stepwise reduction in accelerating voltage from 30 kV to 5 kV and beam currents from 8 nA to 2 pA to minimize Ga^+ ion-induced damage.

The $Fe_{85.2}Si_{0.5}B_{9.5}P_4Cu_{0.8}$ (at. %) metallic glass, also produced as a ~25 mm wide and ~20 μm thick ribbon by melt spinning on a copper wheel, was similarly processed into TEM lamellae using FIB. The

specimen was thinned into a wedge-shaped geometry, resulting in an electron-transparent region with a thickness gradient ranging from approximately 20 nm to 100 nm. Thinning was conducted under the same low-damage FIB protocol as above. The local thickness of the FIB-prepared lamellae was determined via energy-filtered TEM (EFTEM), using the log-ratio method with an estimated inelastic mean free path of 30 nm for 300 kV electrons. The thickness maps of both samples are shown in Figure S3.

2.4. SAED and NBED measurements

Conventional SAED patterns were collected using a Thermo Fisher Scientific Titan G1 80–300 operated at 300 kV with nominally parallel illumination created by well-calibrated 3 condenser lenses and a camera length of 245 mm for $Pd_{80}Si_{20}$. For $Fe_{85.2}Si_{0.5}B_{9.5}P_4Cu_{0.8}$ metallic glasses, SAED patterns were collected using a Thermo Fisher Scientific Themis Z TEM under identical operating conditions.

4D-STEM experiments were conducted for the $Fe_{85.2}Si_{0.5}B_{9.5}P_4Cu_{0.8}$ metallic glass in microprobe STEM mode using a spot size of 7 and a 30 μm C2 aperture with a varying semi-convergence angle range of 0.46–0.84 mrad. The exact value is adjustable by the zoom of the C2 and C3 condenser lenses. This produced a probe with ~1.4–2.6 nm diameter on the sample. For each 4D-STEM dataset, the probe was scanned over a 2D grid (typically 128×128 raster points with ~1.2 nm step size), and a diffraction pattern was collected at each point with an exposure time of 4 ms. Diffraction patterns were recorded using a Merlin pixelated detector (Medipix-based, 256×256 pixel array, Quantum Detector Ltd) and, in some cases, a Gatan OneView camera for higher pixel counts (2048×2048). The reciprocal space sampling (diffraction camera length of 195 mm for the Merlin detector) was chosen such that the maximum scattering angle captured was $k \sim 3$ Å^{-1} sufficient to include the first few diffuse rings of the amorphous diffraction pattern.

2.5. PDF calculations

The diffraction patterns were integrated azimuthally to obtain radial profiles I(k), where the scattering vector $k = 2\sin(\theta)/\lambda$, θ is half of the scattering angle, and λ is the wavelength of the incident electrons. The intensity was then normalized to produce the coherent elastic structure factor ($S(k)$). This was done by subtracting the total atomic scattering factor and normalizing by it. In practice, we calculated an average atomic scattering factor $\langle f(k)^2 \rangle$ based on the alloy composition. The $S(k)$ was then obtained as

$$S(k) = \frac{I(k) - N < f(k)^2 >}{N\langle f(k)^2 \rangle} k,$$

where N is the number of atoms within the volume sampled by the electron probe (determined by fitting $\langle f(k)^2 \rangle$ at k_{max}), and $f(k)$ is the parameterized electron scattering factor for a single atom and is calculated based on Weickenmeier and Kohl [39] proposed formular and documented in Kirkland E. J.'s book [40]. We assumed a uniform distribution of all elements in the sample for calculating the S(k), which is in good agreement with EELS elemental maps for Fe and B for $Fe_{85.2}Si_{0.5}B_{9.5}P_4Cu_{0.8}$ metallic glass (Figure S4), where no indication of elemental segregation was observed.

In disordered materials, multiple scattering does not produce sharp extra peaks in I(k) [41]; instead, it manifests mainly as a low-frequency smooth background under coherent scattering intensity [29]. The experimentally measured $S(k)$ therefore contains a slowly varying background arising from residual multiple and inelastic scattering, such as plasmon tails or diffuse thermal scattering. These contributions do not carry structural information but manifest as a smooth, low-frequency curvature in reciprocal space. If uncorrected, this background propagates into the PDF as baseline shift and artificial short-range features. To compensate for this effect, we applied a low-order polynomial subtraction to model and remove the slowly varying background while preserving the oscillatory components of $S(k)$. This treatment is physically motivated as inelastic and to some extend multiple scattering vary smoothly with scattering angle, whereas structural correlations give rise to high-frequency modulations in $S(k)$. The polynomial function acts as a smooth empirical approximation to the non-structural background, consistent with previous ePDF practices [20,23,25,26].

The choice of polynomial order is not arbitrary but determined by assessing baseline flattening and the stability of the first-shell peak in ePDF. In this work, we systematically examined polynomial orders from first to ninth and adopted the lowest order that effectively removed the smooth curvature without distorting the structural signal. A detailed quantitative discussion, including order-selection criteria and their influence on the resulting PDFs, is provided in Section 3.2. After background correction, the ePDF was obtained by Fourier transforming $S(k)$ using a sine form:

$$g(r) = \int_0^{k_{max}} S(k)\sin(2\pi kr)dk,$$

where k_{max} is the maximum scattering vector included. A Hann function was applied to smoothly bring $S(k)$ to zero at k_{max} to reduce Fourier ripples in PDFs. We also varied k_{max} or the onset of the Hann window (k_{onset}) to test their influence on the resulting PDFs.

3. Results and discussion

3.1. Ground-truth PDF from simulated atomic structures

Fig. 1a shows the atomic configuration of the MD-simulated $Pd_{80}Si_{20}$ glass. From this structure, both the total aPDF and the partial aPDFs for Pd–Pd, Pd–Si, and Si–Si atomic pairs were computed by directly counting the atoms in the model (Fig. 1b). The first peak in the Pd–Si partial aPDF appears at 2.414 Å, and the first Pd–Pd peak is located at 2.745 Å. As shown in the total aPDF, the Pd–Pd correlations dominate due to the high concentration of Pd atoms in the alloy. In contrast, the Si–Si contribution is barely seen, as the Si atoms are sparsely and irregularly embedded within the Pd-rich matrix, which reduces the probability of Si–Si pairing at short distances.

Partial and total $S(k)$ and PDFs were simulated under kinematic conditions using the Debye scattering formula (Fig. 1c and d). The resulting $S(k)$ shows pronounced fluctuations even at high k. The corresponding kPDFs were calculated using a limited k-range up to 2.1 Å^{-1} to match experimental conditions, where the diffraction patterns suffer from limited signal at high k. In our diffraction-based kPDF, a zero baseline represents the average atomic density, with negative values indicating pair correlations below the average. While the peak positions remain consistent with those from the reference aPDF, the peaks appear broadened and suppressed compared to the aPDFs directly counted from the atomic model due to k-space truncation. The coordination number (CN) was calculated from the total PDF over the radial range of 2.0 Å to 3.3 Å using the integral expression

$$CN = \int_{r_0}^{r_1} 4\pi r^2 g(r)dr.$$

For the directly counted aPDF, the resulting CN is 13.22. For the kPDF evaluation, the baseline was defined by locating the first minimum preceding the first peak. This determination of baseline introduces some variation in the calculated CN values, yielding 12.92 for the kPDF. Despite these differences, the CN values remain within a comparable range and align well with the typical coordination environments (CN ≈ 13) expected for Pd-Si metallic glasses [42].

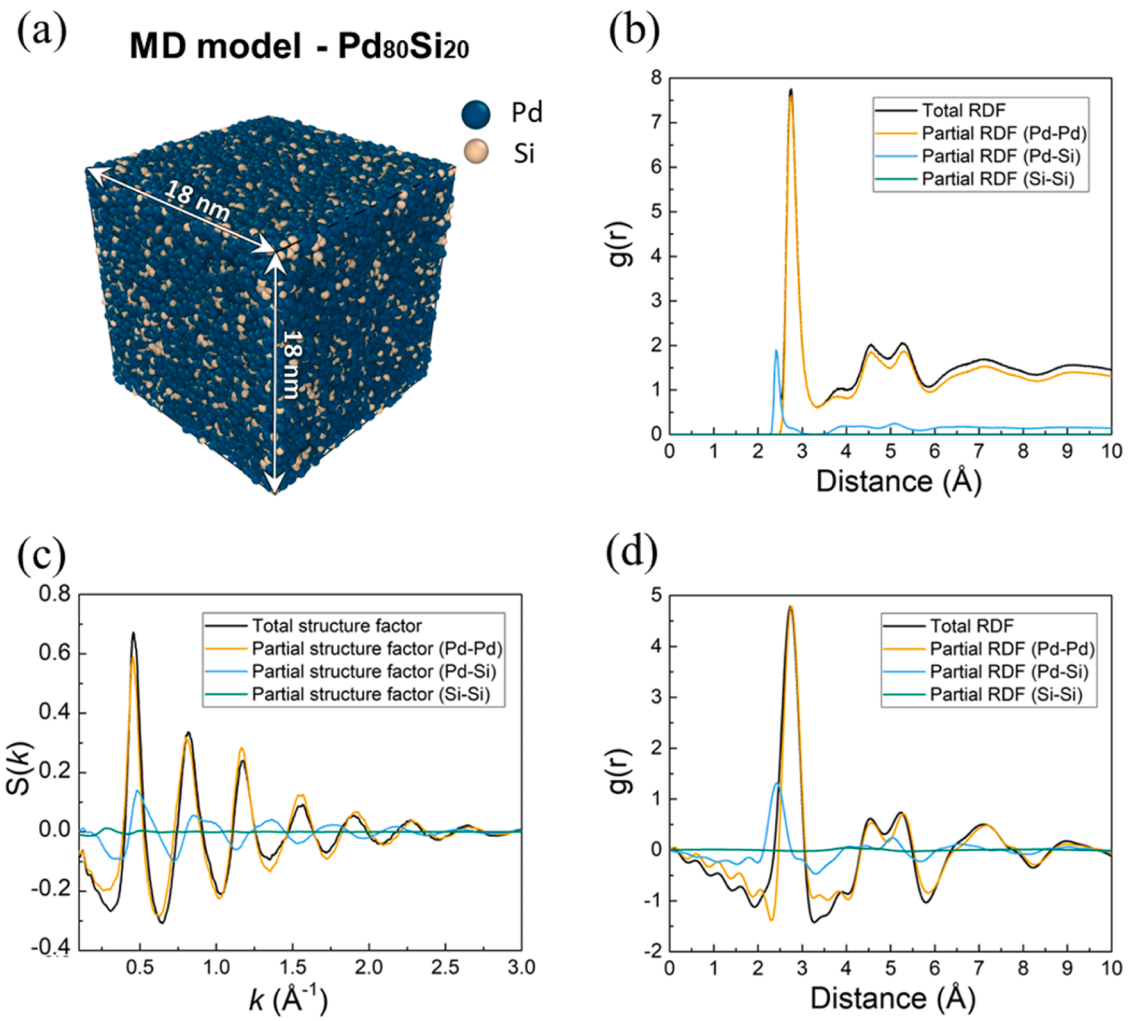

Fig. 1. Ground truth PDFs generated from counting atomic distances and based on kinematic diffraction simulation. (a) The atomic structure model of the $Pd_{80}Si_{20}$ metallic glass obtained from MD simulation. (b) PDF by counting atomic distances directly in the MD model (aPDF). (c) Kinematic *S(k)* from the Debye scattering simulation. (d) ePDF from the kinematic simulation (kPDF).

3.2. Influence of sample thickness and multiple scattering on ePDF calculation

We assess the impact of multiple scattering on the fidelity of the ePDF by simulating electron diffraction for varying sample thickness using multi-slice algorithms based on a stacked atomic model. Simulated SAED patterns corresponding to thicknesses of 20 nm, 40 nm, 60 nm, and 100 nm are shown in Fig. 2b As thickness increases, the diffraction rings become progressively more diffuse and blurred due to increased multiple scattering and reduction in the coherent signal-to-background ratio. $f(k)$ often does not perfectly match the experimental $I(k)$ across small and large angles simultaneously due to contributions from multiple scattering (Fig. 2c). This deviation induces a low-frequency background in *S(k)* as shown in Fig. 2d The corresponding ePDFs obtained from the Fourier sine transformation of this *S(k)*s are shown in Fig. 2f. Without any baseline subtraction, the ePDF exhibits artificial peaks at small $r < 2$ Å due to residual multiple scattering contributions. To suppress these effects, polynomial fitting was applied to isolate and subtract the low-frequency background component from the raw *S(k)* data, following previous works [20,23,25,26]. Simply cropping the ePDF at $r < 1$ Å can hide the most visible artifacts but does not correct the baseline of *S(k)*, which can further exacerbate biases in peak position and introduce fluctuations at larger r in the PDF. In thicker samples, where multiple scattering becomes more significant, such baseline distortions are even more pronounced and cannot be effectively removed by simple truncation.

Fig. 2e presents *S(k)* after fourth-order polynomial baseline correction, which effectively removes low-frequency fluctuations from multiple scattering. This also eliminates the artificial ePDF peak at short distances below 2 Å (Fig. 2*g*). The polynomial order was systematically varied (1st–9th) to avoid overfitting (Figure S2); we choose the lowest order that flattens the *S(k)* baseline without distorting oscillations or shifting the first PDF peak by more than ±0.005 Å. Subtracting a too high-order polynomial background from *S(k)* can cause overfitting problems, which alter the physically meaningful oscillations related to atomic correlations. Therefore, the use of polynomial fitting and the choice of its order must be carefully evaluated to avoid compromising meaningful structural features. In practice, a 4th-order polynomial correction is required for thicker samples without deconvolution to adequately suppress the artificial low-r peak. To systematically assess this effect, polynomial baseline corrections of varying orders (1–9) were applied to *S(k)*, and the resulting ePDFs were analyzed. In particular, the first ePDF peak position was tracked as a function of polynomial order (Figure S2). At a constant sample thickness, the peak positions remain stable up to the 5th-order correction. However, higher-order fitting (beyond 6th order) introduces noticeable fluctuations in the peak position, indicating a loss of coherent structural signal due to overfitting.

Even with an appropriately chosen polynomial correction, the result

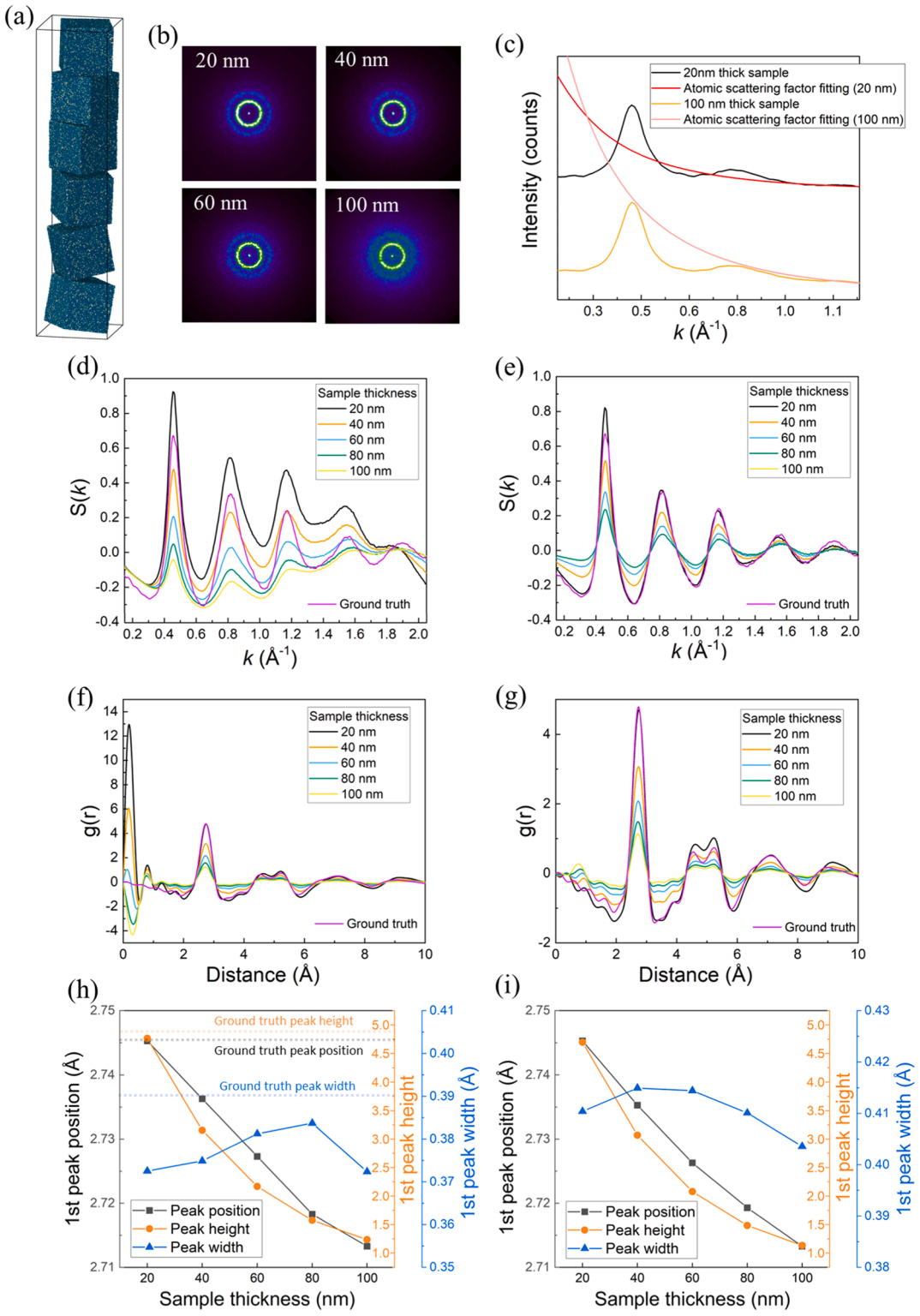

Fig. 2. Effect of multiple scattering on dynamic diffraction analysis. (a) Stacked atomic models of $Pd_{80}Si_{20}$ used to simulate increasing sample thickness. (b) Simulated SAED patterns for thicknesses of 20, 40, 60, and 100 nm based on multi-slice simulation. The 100 nm sample shows significantly broadened and diffuse rings due to intensified multiple scattering. (c) Radial intensity profiles and fitted atomic scattering factors for the 20 nm and 100 nm models. The 20 nm case aligns well with the fit, while the 100 nm model shows notable deviations caused by multiple scattering artifacts. (d) Structure factor *S(k)* calculated from simulated patterns for thicknesses of 20, 40, 60, 80, and 100 nm. The low-frequency background varies with thickness due to multiple scattering. (e) *S(k)* after fourth-order polynomial baseline correction. (f) ePDFs before baseline correction, calculated with a *S(k)* window of 0.2–2.05 $Å^{-1}$, $\Delta k = 0.005$ $Å^{-1}$ and a convergence angle of 0 mrad. (g) ePDFs after fourth-order polynomial baseline correction (calculated with the same Fourier transform window and convergence angle conditions). (h) First peak position, intensity, and FWHM of the ePDF (without polynomial correction) plotted against sample thickness. (i) First peak position, intensity, and FWHM of the ePDF (after fourth-order correction) plotted against sample thickness.

shows a gradual shift of the peak position towards lower values with increasing sample thickness (Fig. 2i), showing no significant improvement compared to the uncorrected case (Fig. 2h). Previous studies and our simulations demonstrate that multiple scattering redistributes electrons toward higher scattering angles, resulting in noticeable shoulders on all diffracted peaks [29,41]. Consequently, the measured first peak position decreases by approximately 1.2 % as the sample thickness increases from 20 nm to 100 nm, accompanied by a reduction in the first peak intensity and a nonlinear variation in its width.

To address the physical origins of multiple elastic scattering, we employed an analytical deconvolution approach based on the formalism presented by Anstis et al. [29] and Ankele et al. [41] The multiple scattering intensity I(k) is expressed as multiple single scattering with distribution $\Psi(k)$, where each $\Psi(k)$ is fulfilling the single scattering approximation, leading to

$$\mathrm{I}(k) = \mathrm{I}_0\left[\delta(k) + \mathrm{Z}\Psi(k) + \frac{\mathrm{Z}^2}{2!}\Psi(k)*\Psi(k) + \cdots\right]\mathrm{e}^{-\mathrm{Z}/\Lambda},$$

where Z is the specimen thickness, Λ is the elastic mean free path, and * denotes two-dimensional convolution. Assuming azimuthal symmetry in a sufficient volume of amorphous materials, the expression is simplified using a Fourier-Bessel transform to convert I(k) to real space

$$\mathrm{I}(\mathrm{r}) = 2\pi\int_0^\infty \mathrm{I}(k)k\mathrm{J}_0(2\pi\mathrm{r}k)\mathrm{d}k.$$

The inverse operation enables the retrieval of the effective single scattering distribution as

$$\Psi(\mathrm{r}) = \frac{1}{\mathrm{Z}}\ln\left(\frac{\mathrm{I}(\mathrm{r})}{\mathrm{I}_0}+1\right) + \frac{1}{\Lambda},$$

assuming a Poisson distribution of scattering events. From this, the corrected reciprocal-space intensity I(k), representing predominantly single-scattering events, is recovered by applying the inverse Fourier-Bessel transform to S(r).

Fig. 3 presents the deconvolution results of diffraction patterns for the $Pd_{80}Si_{20}$ models with thicknesses of 20, 40, 60, 80, and 100 nm. After the correction, the shift of the shoulders of the *S(k)* peaks towards higher scattering angles is effectively eliminated. The position of all PDF peaks is consistent across the entire thickness range, where the first nearest-neighbor distance at 2.745 Å can be measured accurately for thick specimens. Furthermore, the oscillations of *S(k)* become comparable across all sample thicknesses and are close to the correct zero baseline. The more linear background results in a lower order (1st to 3rd) polynomial used for background removal. Fig. 3d presents the variation of the first ePDF peak position, intensity, and FWHM as a function of sample thickness after third-order polynomial correction. The peak position stays at 2.745 ± 0.001 Å across all thicknesses, in excellent agreement with the ground truth PDF. Furthermore, the variation of the peak intensity and the peak width with increasing thickness is reduced very significantly (Fig. 3d). These findings verify the 2D self-convolution mechanism as the strongest physical origin for the multiple scattering effects in ePDF analysis. This procedure not only reduces the error in coordination number estimation (i.e., peak intensity attenuation) resulting from multiple elastic scattering, but also results in accurate interatomic distances measured by the pair distribution function.

Although the deconvolution approach is successful, it requires prior knowledge of the sample thickness and the elastic scattering mean free

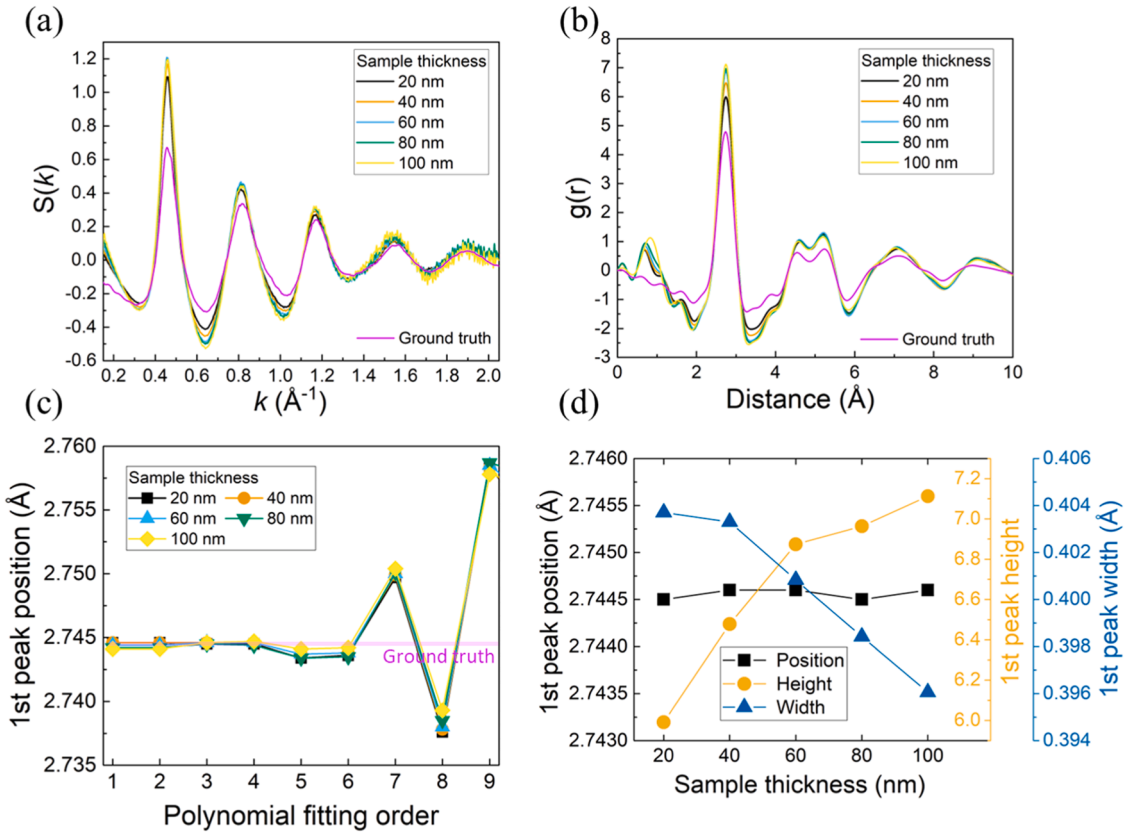

Fig. 3. Compensation for multiple scattering by deconvolution (a) *S(k)* for $Pd_{80}Si_{20}$ models with thicknesses of 20, 40, 60, 80, and 100 nm, after deconvolution and third-order polynomial background correction. (b) Corresponding ePDFs for selected thicknesses, calculated with a *S(k)* window of 0.2–2.05 Å^{-1}, Δk = 0.005 Å^{-1} and a convergence angle of 0 mrad. (c) First peak position of the ePDF as a function of polynomial fitting order. (d) First peak position, intensity, and FWHM of the ePDF (after third-order correction) plotted against sample thickness.

path, which are not trivial to determine. In particular, the elastic scattering mean free path is a phenomenological parameter rather than a physical quantity derived from the wave–potential interaction. Inaccurate estimation of these two parameters can lead to overcorrection. In contrast, the polynomial fitting approach is capable of eliminating low-frequency artifacts with some tolerance to measurement uncertainties. Therefore, the polynomial fitting approach provides a more practical and robust means of suppressing the multiple scattering effect in the PDF. In practice, when measurements are performed on samples with comparable thicknesses, the thickness-induced shift in peak position is relatively minor and does not significantly affect the overall analysis.

3.3. *Effect of Fourier transformation window: maximum scattering angle and handling of zero beam on ePDF*

The range of scattering angle included in the Fourier sine transform for the ePDF procedure, characterized by the upper limit k_{max}, directly governs the real-space resolution of the resulting PDF, as described by the relation $\Delta r \approx \frac{1}{k_{max}}$. In practice for electron diffraction, k_{max} is constrained by the angular coverage of the microscope optical alignment of the crossover at the differential pump aperture above the projection chamber, detector size, and the SNR at high scattering angles. To focus on the evaluation of the influence of k_{max}, simulations were performed using the thin-sample $Pd_{80}Si_{20}$ model (20 nm), wherein the *S(k)* was artificially truncated at different k_{max} values to mimic varying angular acquisition limits. Fig. 4a shows the truncated *S(k)* with cutoffs corresponding to the fifth amorphous diffraction ring (2.05 $Å^{-1}$), fourth ring (1.704 $Å^{-1}$), abrupt termination within the fourth ring (1.55 $Å^{-1}$), third ring (1.4 $Å^{-1}$), and second ring (1 $Å^{-1}$). The resulting ePDFs are shown in Fig. 4b When only the second diffraction ring is included, the ePDF is severely limited in real-space detail; only the nearest-neighbor peak is visible at the identical position, while the second peaks are merged into a featureless background. Extending the range to include the third diffraction ring (k_{max} =1.3 $Å^{-1}$) yields a substantially improved ePDF, well matching the ground truth PDF, with fine details of high-order peaks at 4–8 Å. A further increase of k_{max} beyond this point shows a limited gain in the fine peaks, though it reduces the Fourier ripples induced artifacts. As the same to the high-energy X-ray and neutron PDF studies [43], extending k_{max} into the higher-angle regime enables improved real-space resolution by incorporating higher-frequency structural information. This is particularly critical for crystalline materials with well-defined and closed interatomic correlation spacings. In such systems, the *S(k)* does not decay fast enough at high *k*, therefore introducing a strong rippling effect from the Fourier transform. For glasses, and other structurally disordered materials, the gain of acquiring high-*k* coverage is significantly reduced, because the highly fluctuated interatomic distance makes that the *S(k)* reduces fast at the high angle, thereby reducing the sensitivity of the PDF to the Fourier

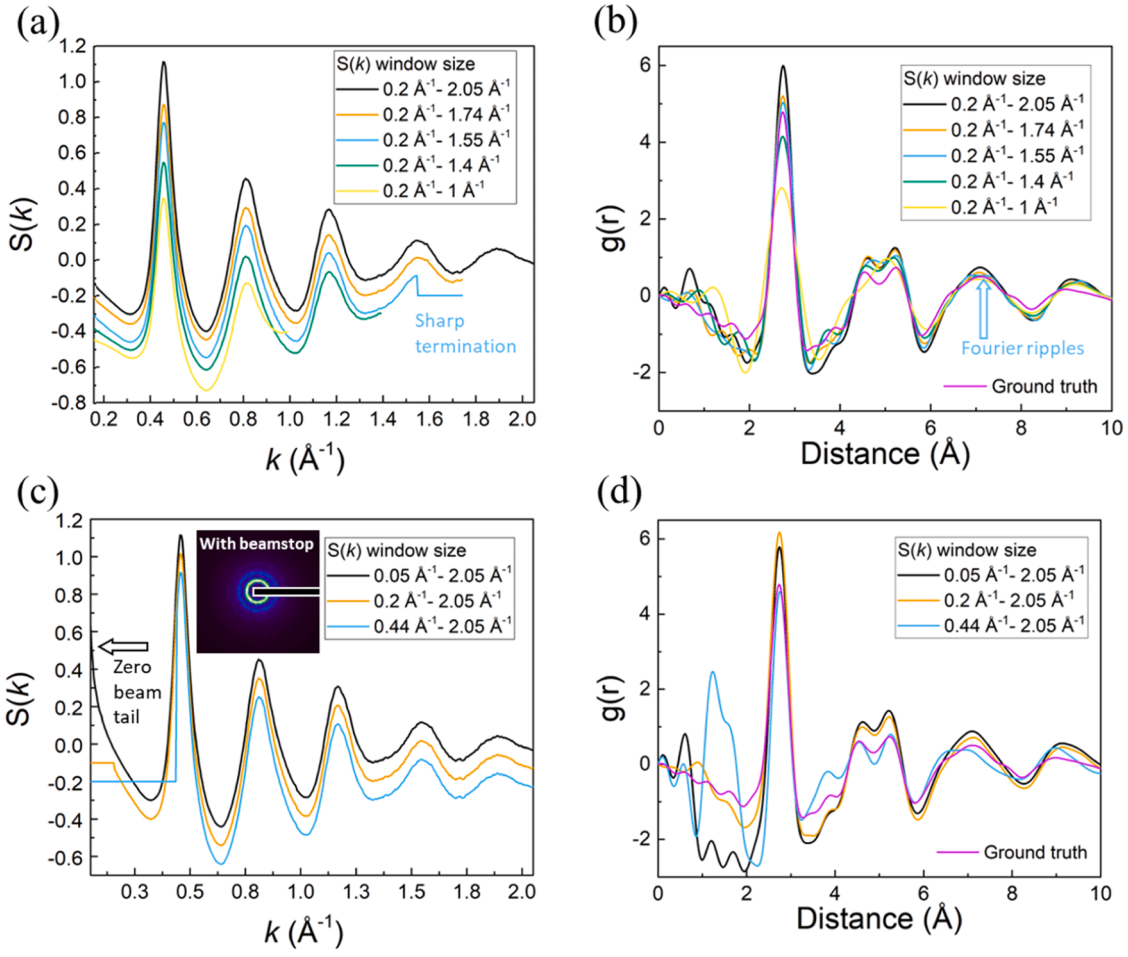

Fig. 4. Effect of maximum scattering angle and treatment of the central beam on ePDF calculations. SAED patterns of the $Pd_{80}Si_{20}$ model were simulated for a 20 nm thick sample. (a) *S(k)* calculated with a convergence angle of 0 mard and varying cutoffs for the maximum scattering vector, reflecting different angular limits. (b) Corresponding ePDFs obtained from the *S(k)* data shown in (a), calculated with varying Fourier transform windows, $\Delta k = 0.005$ $Å^{-1}$, a convergence angle of 0 mrad, and after applying deconvolution and third-order polynomial baseline correction, illustrating the impact of *S(k)* window size on ePDF. (c) *S(k)* generated with different onset values for the *S(k)* window function, representing different treatments of the central beam (beamstop region). (d) Corresponding ePDFs derived from the *S(k)*s in (c) and after applying deconvolution and third-order polynomial background correction, showing the influence of low-*k* cutoff.

transformation truncation artifacts in the high-k regime [7]. In the case of the exemplary metallic glasses, low k_{max}, e.g. 1.3 Å^{-1}, can yield reasonable ePDF with accurate short- and medium-range structural information.

The side at the small scattering angle (low-k regime) relates to the material that exhibits large-scale density fluctuations, such as in porous frameworks or phase-separated nanostructures. Proper treatment of the low-k region is also critical for reliable ePDF interpretation. The intense direct electron beam, typically blocked by a beamstop to avoid detector saturation, results in the exclusion of low-k scattering data. This missing region can introduce baseline distortions and spurious low-frequency artifacts in the ePDF. To evaluate the sensitivity of the ePDF to k_{onset}, three scenarios were tested: (i) $k_{onset} = 0.05$ Å^{-1}, including the tail of the central beam; (ii) $k_{onset} = 0.2$ Å^{-1}, simulating partial masking of the zero beam; and (iii) $k_{onset} = 0.4$ Å^{-1}, representing a large beamstop that blocks major part of the first diffraction ring. The corresponding *S(k)*s and ePDFs are shown in Fig. 4c and 4d Although the 1st peak positions in the ePDFs remain similar across all three cases, the geometrical functions differ significantly. Especially, setting k_{onset} to 0.4 Å^{-1}, which removes the major part of the 1st diffraction ring, causes a loss of essential low-frequency information and results in termination artifacts in the final ePDF. Among the three, the condition of $k_{onset} = 0.2$ Å^{-1} combined with $k_{max} = 1.3$ Å^{-1} yields the most reliable ePDF that closely matches the reference. These results demonstrate that accurate and artifact-free ePDF reconstruction requires rational selection of k_{max} and k_{onset}.

3.4. *Influence of resolution in reciprocal space on ePDF calculation*

Fig. 5 shows the effect of the probe convergence semi-angle (α) and the angular resolution of the diffraction pattern on the ePDF. A larger α produces a more convergent beam, giving that each diffraction feature is convolved with the probe-forming aperture function (roughly a disk of semi-angle α). This convolution leads to a reduced angular resolution, manifesting itself as a blurring of fine features in the diffraction pattern. To isolate the impact of α, simulations were performed using the $Pd_{80}Si_{20}$ model under thin-sample conditions, with α varied from parallel to 1.5 mrad. Fig. 5a presents the background-corrected *S(k)*s corresponding to selected convergence angles. At small α (0–0.6 mrad), *S(k)* retains sharp oscillations characteristic of high angular resolution. However, as α increases beyond 0.9 mrad, these oscillations diminish, indicating a progressive loss of high-frequency structural contrast in reciprocal space. The real-space implications of this angular blurring are reflected in the corresponding ePDFs shown in Fig. 5b While the position of the first peak remains consistent across all convergence angles, a notable reduction in its intensity is observed under NBED conditions. Moderate

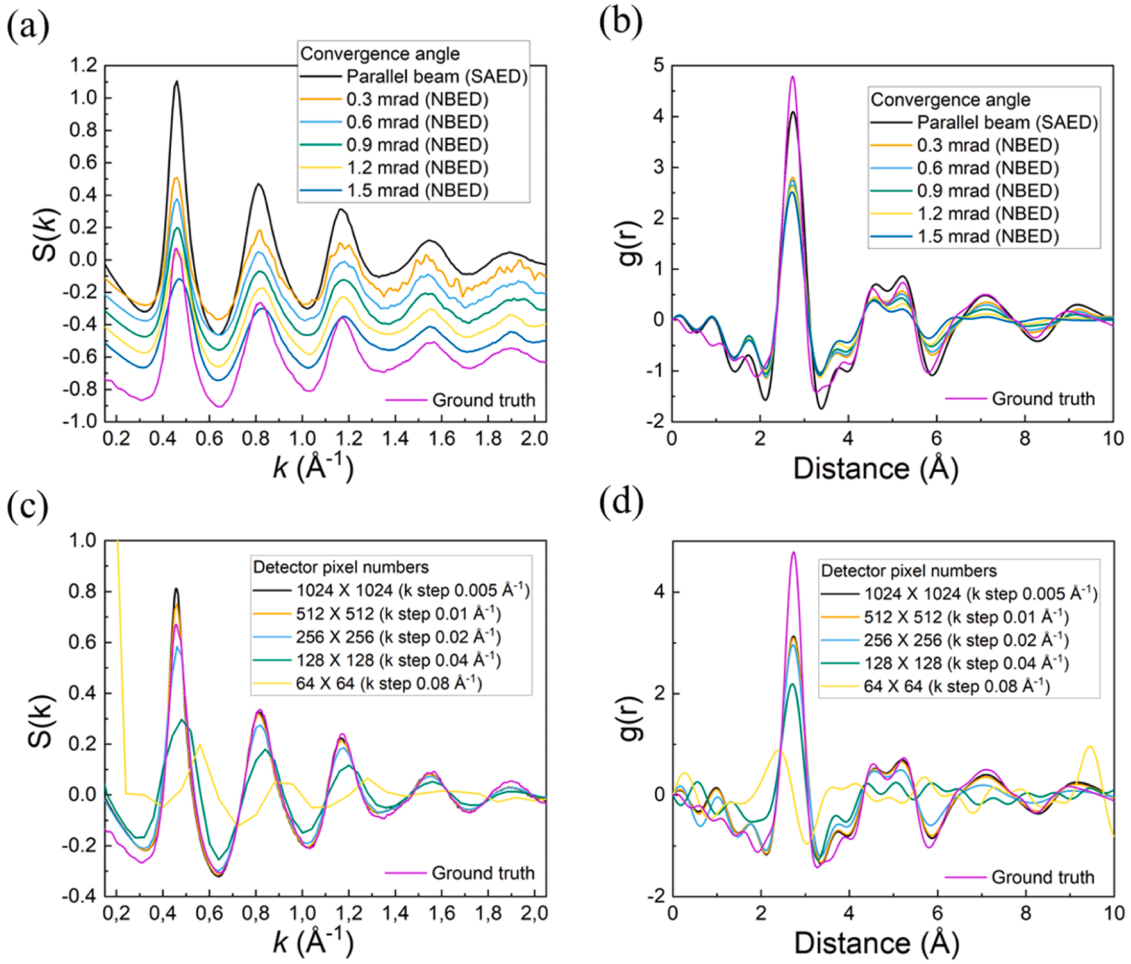

Fig. 5. Effect of resolution in reciprocal space on ePDF calculation. (a) *S(k)*s of the $Pd_{80}Si_{20}$ glass model computed using different convergence semi-angles of the electron beam, ranging from 0 to 1.5 mrad. SAED optical setting was applied for the parallel condition. For the convergent beam, the NBED optical setting was applied. (b) Corresponding ePDFs derived from the *S(k)*s in (a) After applying deconvolution and third-order polynomial baseline correction, an S(k) window of 0.2–1.3 Å^{-1} was used in the ePDF calculation to emulate a typical 4D-STEM experiment and suppress noise contributions at high k. (c) *S(k)*s obtained from an NBED (convergence angle of 0.6 mrad) for different detector pixel numbers: 1024×1024, 512×512, 128×128, and 64×64 corresponding to k step sizes of 0.01, 0.02, 0.04, and 0.08Å^{-1}. (d) Corresponding ePDFs calculated from the binned data in (c) after applying deconvolution and third-order polynomial baseline correction, using the same *S(k)* window as in (b).

convergence angles (α = 0.3–0.6 mrad) result in the attenuation of peak height but still preserve distinct first and second coordination peaks at correct positions. In contrast, large convergence angles (α > 0.9 mrad) lead to significant degradation of medium-range structure, including loss of detail in the shoulder region between the second and third peaks. At α = 1.5 mrad, the PDF becomes highly broadened, with little structural distinction beyond the first coordination shell.

Angular broadening in the reciprocal space is mathematically identical to multiplying a dampening function, which is the Fourier transform of the broadening function, in the PDF. In addition, the large convergence angle of the electron probe leads to a smaller real-space probe size, which limits sensitivity to long-range interatomic correlations. This further suppresses high-frequency components, thereby reducing the intensity of the peaks. This indicates the importance of using a small convergence angle to preserve ePDF fidelity, particularly for resolving medium-range order. This necessitates operating the TEM in nanobeam or parallel beam diffraction mode, where sufficiently small convergence angles are achievable. From a practical standpoint, a convergence angle of 0.6 mrad (for materials with nearest interatomic distances longer than 2.5 Å) was used as the standard condition for subsequent NBED simulations and experiments. This trade-off becomes particularly critical in 4D-STEM ePDF experiment, where the primary goal is often to map local structural variations by scanning a fine probe across the sample. Achieving high spatial resolution (a small probe) typically requires a larger convergence angle. However, as our results show, increasing the convergence angle degrades the ePDF quality by reducing angular resolution and dampening real-space features. Therefore, a single NBED pattern in a 4D-STEM scan represents the average structure within the nanometer-scale volume illuminated by the probe. Capturing genuine structural variations requires comparing ePDFs from different probe positions. The choice of convergence angle is thus a crucial compromise: it must be small enough to preserve the fidelity of key structural features in the ePDF, yet large enough to form a probe suitable for spatially-resolved mapping.

The quality of ePDF can also be constrained by the angular sampling of the diffraction pattern, which is governed by the detector pixel count or, equivalently, the degree of binning applied during acquisition or post-processing. Insufficient angular sampling can introduce aliasing, where high-frequency features in the *S(k)* are undersampled, leading to degraded information in the resulting ePDF. To quantitatively assess the effect of angular sampling, high-resolution diffraction data simulated from the $Pd_{80}Si_{20}$ model (originally computed on a grid with 1024×1024 pixels) were systematically down-sampled to emulate detectors with lower effective pixel sampling. The data were re-binned to grids of 512×512, 256×256, 128×128, and 64×64 pixels corresponding to pixel sizes of 0.01, 0.02, 0.04, and 0.08Å^{1}, with all cases covering the same scattering vector range. Fig. 5c shows *S(k)*s derived from these down-sampled datasets with different detector pixel numbers and sizes. For detector sizes of 1024×1024, 512×512, and 256×256 pixels, *S(k)* retains well-defined oscillatory features and smooth profiles across the full *k*-range. In contrast, significant distortion is evident in the 128×128 and especially 64×64 cases, and aliasing appears as a consequence of undersampling. Fig. 5d shows the corresponding ePDFs. For detector sizes of 256×256 pixels and above, the ePDFs accurately reproduce both the positions and relative intensities of real-space features, except for the dampening at longer interatomic distances. At 128×128 and 64×64 resolution, the first peak exhibits a noticeable reduction in intensity and a shift in position. Peaks beyond the first coordination shell become increasingly unreliable. These results demonstrate that the accuracy of ePDF reconstruction is primarily governed by the reciprocal-space sampling density, which depends on both the pixel size (in Å^{-1}) and the total sampling range in *k*-space. In this study, an effective pixel size of 0.02 Å^{-1} or finer (corresponding to 256×256 pixels over the given angular range) was sufficient to preserve the structural fidelity of the ePDF for the $Pd_{80}Si_{20}$ model. However, this threshold is not universal. Materials with shorter interatomic distances exhibit lower-frequency oscillations in *S(k)*, allowing accurate reconstruction even with coarser sampling (e.g., 128×128 or 64×64 pixels), provided that the Nyquist criterion is satisfied. Conversely, materials with longer bonds or more complex local structures require finer sampling. Ensuring adequate *k*-space resolution relative to the characteristic structural frequencies is essential for reliable ePDF analysis. In practical terms, modern 4D-STEM detectors offering 256×256 or 512×512 pixel formats generally provide sufficient resolution for a broad class of materials, but smaller frame sizes or further down-sampling must be carefully evaluated on a case-by-case basis.

3.5. Effect of noise and electron beam precession

Electron dose is a critical factor for ePDF analysis, as it directly affects the SNR of diffraction patterns, especially at large scattering angles. While higher doses generally improve SNR, they also raise the risk of beam-induced damage, especially in radiation-sensitive materials. Here, we investigate how varying electron dose influences the quality and interpretability of ePDF results by adding Poisson noise to the simulation from the $Pd_{80}Si_{20}$ metallic glass model. Fig. 6a displays the *S(k)*s obtained at three different electron doses: 9000 e$^-$, 90,000 e$^-$, and an effective infinite dose reference. At the lowest dose (9000 e$^-$), *S(k)* exhibits increased noise, particularly in the high-*k* region, leading to poorly resolved oscillatory features. As the dose increases to 90,000 e$^-$, the *S(k)* becomes smoother and more defined, closely resembling the infinite-dose reference. The corresponding ePDFs shown in Fig. 6b further illustrate the impact of dose on real-space structural interpretation. At 9000 e$^-$, the ePDF exhibits notable fluctuations and artificial peaks beyond the first coordination shell (r > 4 Å), due to noise at the large diffraction angle. In contrast, both the 90,000 e$^-$ and infinite-dose datasets yield well-defined ePDFs with consistent peak positions and reduced background ripples. The first and second coordination peaks remain largely consistent for the 90,000 e$^-$ and infinite case, suggesting that short-range structural information is relatively robust. However, higher-range features are significantly compromised due to the low signal. These results demonstrate that ePDF can tolerate some level of noise for short-range analysis, quantitative interpretation of medium- to long-range structural features requires an electron dose to ensure a sufficient information-to-noise ratio in ePDF. For dose-sensitive materials, this highlights the need to optimize dose carefully, balancing beam damage and data quality, or to implement dose-efficient acquisition strategies such as scanning sparsely with high frame averaging or using advanced denoising algorithms.

Electron beam precession is frequently employed in 4D-STEM to mitigate dynamic scattering effects, improve the visibility of weak reflections at high scattering angles, and enhance the overall SNR, particularly in crystalline materials [44]. We investigate the effect of beam precession using simulated NBED patterns for the thin $Pd_{80}Si_{20}$ glass for varying precession angles, 0°, 1°, and 3°, while keeping the total electron dose constant. While precession theoretically averages over multiple beam tilts to better sample the isotropic structure, the resulting changes in the ePDF were found to be minimal (Fig. 6d). This minimal impact is likely because the amorphous structure of the metallic glass is already inherently isotropic, meaning the additional orientational averaging provided by precession offers no significant benefit. Therefore, based on our data, we conclude that beam precession has a negligible effect on the ePDF obtained from this metallic glass system.

3.6. Figure of merit and comparison of experimental conditions

To provide a quantitative and consistent assessment of ePDF quality, we established a three-tiered Figure of Merit (FOM) framework. This framework enables a systematic evaluation of how various experimental and data-processing parameters influence the quantitative accuracy of the ePDF. Specifically, we define: (1) the Scaling Factor (FoM 1) as a measure of the overall normalization and stability of the ePDF intensity.

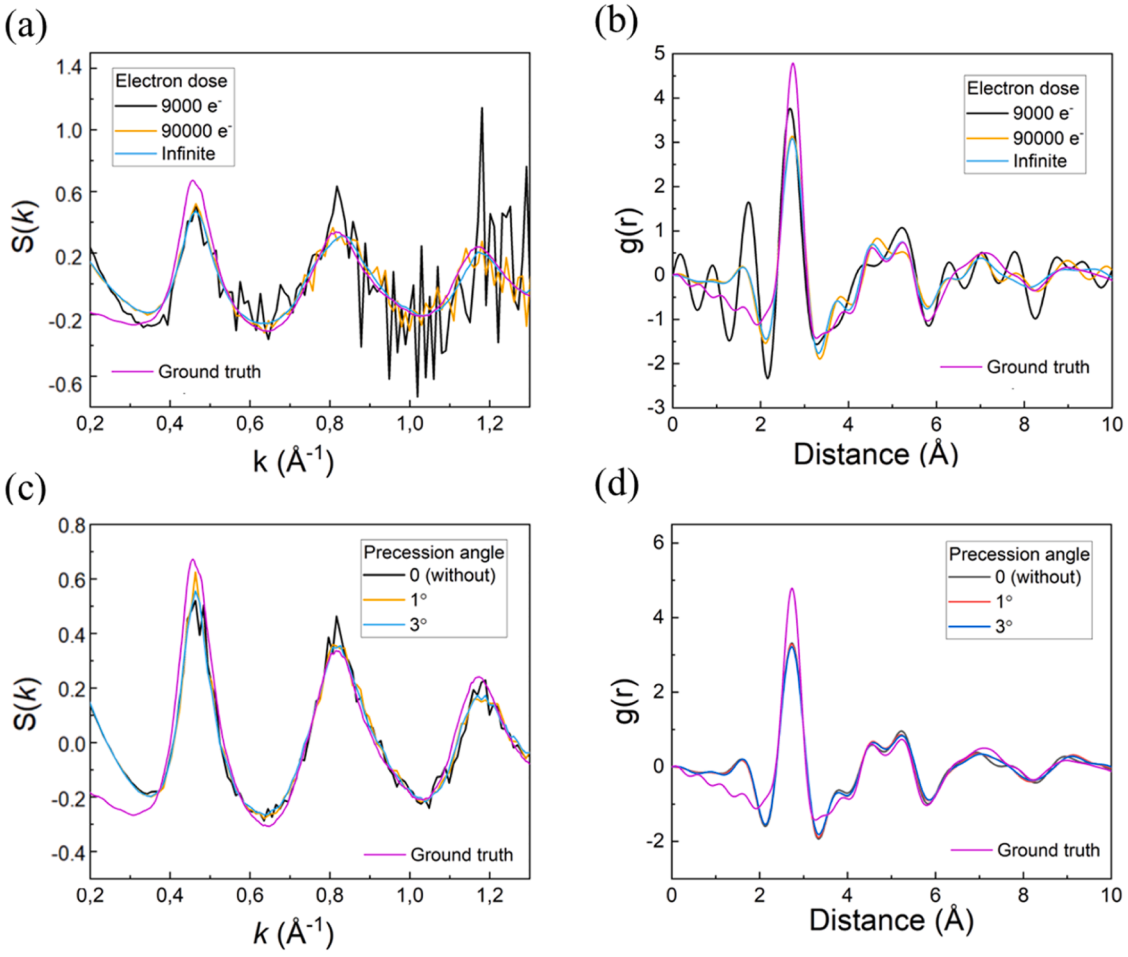

Fig. 6. Effect of electron dose and electron beam precession for ePDF analysis. NBED patterns of the $Pd_{80}Si_{20}$ model were simulated for a 20 nm thick sample with a convergence angle of 0.6 mrad, with varying electron dose and precession angles. (a) *S(k)*with different electron doses of 9000 e^{-}, 90,000 e^{-}, and infinite (b) corresponding ePDFs after applying deconvolution and third-order polynomial baseline correction. A *S(k)* window of 0.2 to 1.3 $Å^{-1}$, $\Delta k = 0.005$ $Å^{-1}$ was applied to the ePDF calculation to avoid the noise contribution at high *k*. (c) *S(k)* from simulated diffractions without, with 1°, and 3° electron beam precession. (d) Corresponding ePDFs of each electron beam precession case after applying deconvolution and third-order polynomial baseline correction, using the same *S(k)* window as in (b).

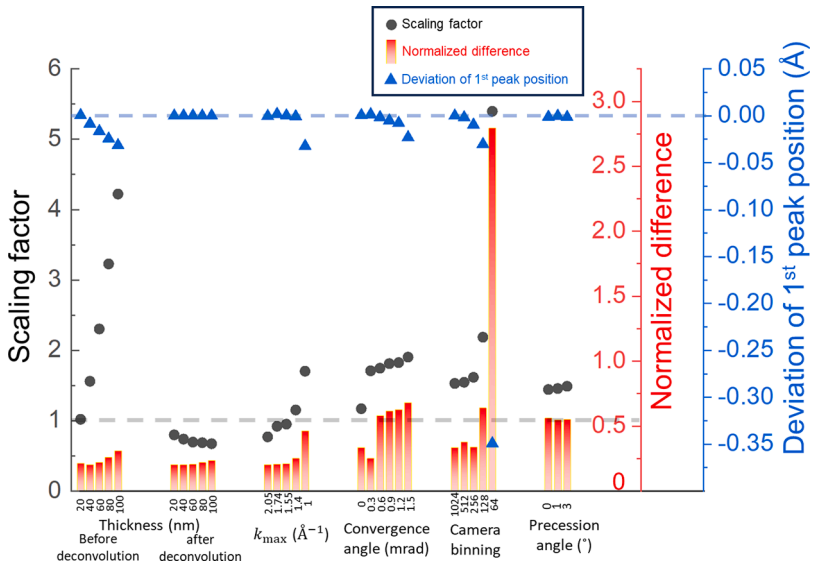

Fig. 7. Summary of how various experimental and data-processing parameters influence the quantitative accuracy of ePDF measurements. The black circles represent the Scaling Factor (left Y-axis), indicating the overall normalization and stability of the ePDF intensity. The red bars correspond to the Normalized Difference (1st right Y-axis, in red), quantifying the overall deviation between the measured and reference kPDF curves and thus reflecting the global curve similarity. The blue triangles represent the Deviation of the First Peak Position (2nd right Y-axis, in blue), which directly evaluates the accuracy of the nearest-neighbor atomic distance. The dashed line indicates the reference information. This chart allows for a comprehensive comparison of how factors like sample thickness, k_{max}, and convergence angle, binning number, and precession impact both the overall curve fidelity and the precision of a key structural parameter.

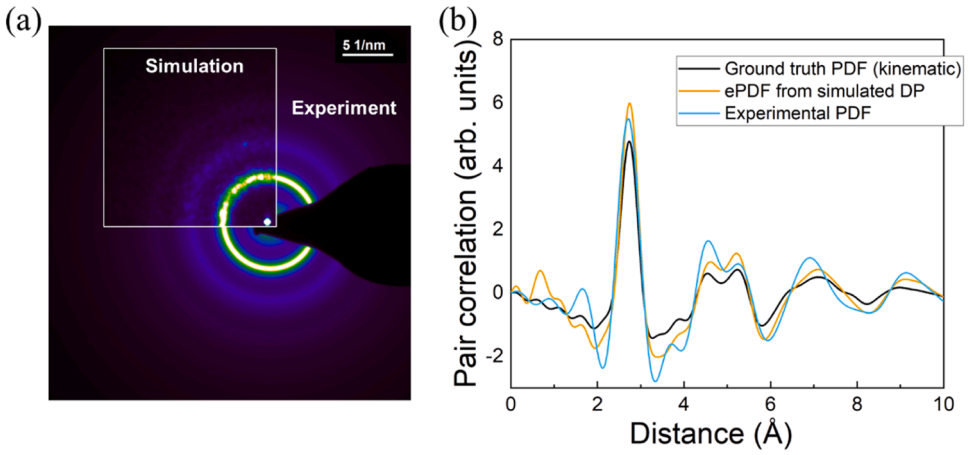

Fig. 8. Comparison of ground truth PDF (reference), ePDF from simulated SAED, and ePDF from experimental SAED. (a) Experimental diffraction pattern of $Pd_{80}Si_{20}$ glass acquired using SAED in TEM. The inset shows a simulated SADP pattern of the $Pd_{80}Si_{20}$ model with 40 nm thick for direct comparison with the experimental data. (b) kPDF derived from the kinematic diffraction pattern; ePDF obtained from simulated SAED after deconvolution and third-order polynomial baseline correction; and experimental PDF from measured SAED. An S(k) window of 0.2–2.1 Å^{-1} was used for both ePDF and experimental PDF.

In this work, the scaling factor is calculated based on the height of the first PDF peak, which provides a robust and physically meaningful reference for comparing different conditions. (2) The Normalized Euclidean Difference (FoM 2) quantifies curve-level similarity between the measured and reference kPDFs. This metric is computed by taking the point-by-point difference after applying the FoM 1–based normalization. In our analysis, the r-range used for the comparison was 2 Å to 8 Å, and the metric was obtained by summing the absolute point-wise differences over this interval. (3) The First-Peak Position Deviation (FoM 3) serves as an indicator of local structural accuracy corresponding to the nearest-neighbor distance. The deviation is reported in angstroms (Å). A summary of these three metrics across all tested conditions is presented in Fig. 7.

Comparison of the values of before- and after-deconvolution indicates that multiple scattering both alters the overall intensity scaling and distorts the local structural features. This highlights a known limitation in ePDF analysis; peak heights and integrated intensities can be sensitive to sample thickness, complicating the quantitative interpretation of atomic coordination or density. For the choice of the maximum scattering vector, k_{max}, when the signal is preserved up to at least the third oscillation, the first-peak position remains accurate and the normalized difference stays low. However, truncating the data at a lower k_{max} results in significant peak broadening, hence cross-talking between adjacent peaks and larger deviations in both FOM 1 and FOM 2, due to the modified Fourier window and altered fitting conditions. Instrumental parameters affecting angular resolution exhibit similar tendencies. Both FoM 1 and FoM 2 show a gradual increase as the convergence angle becomes larger or the detector sampling becomes coarser. These trends reflect a steady degradation in overall data normalization and curve fidelity, while FoM3 remains relatively robust within the experimentally optimized range. Finally, applying beam precession in this amorphous system produced no significant change in

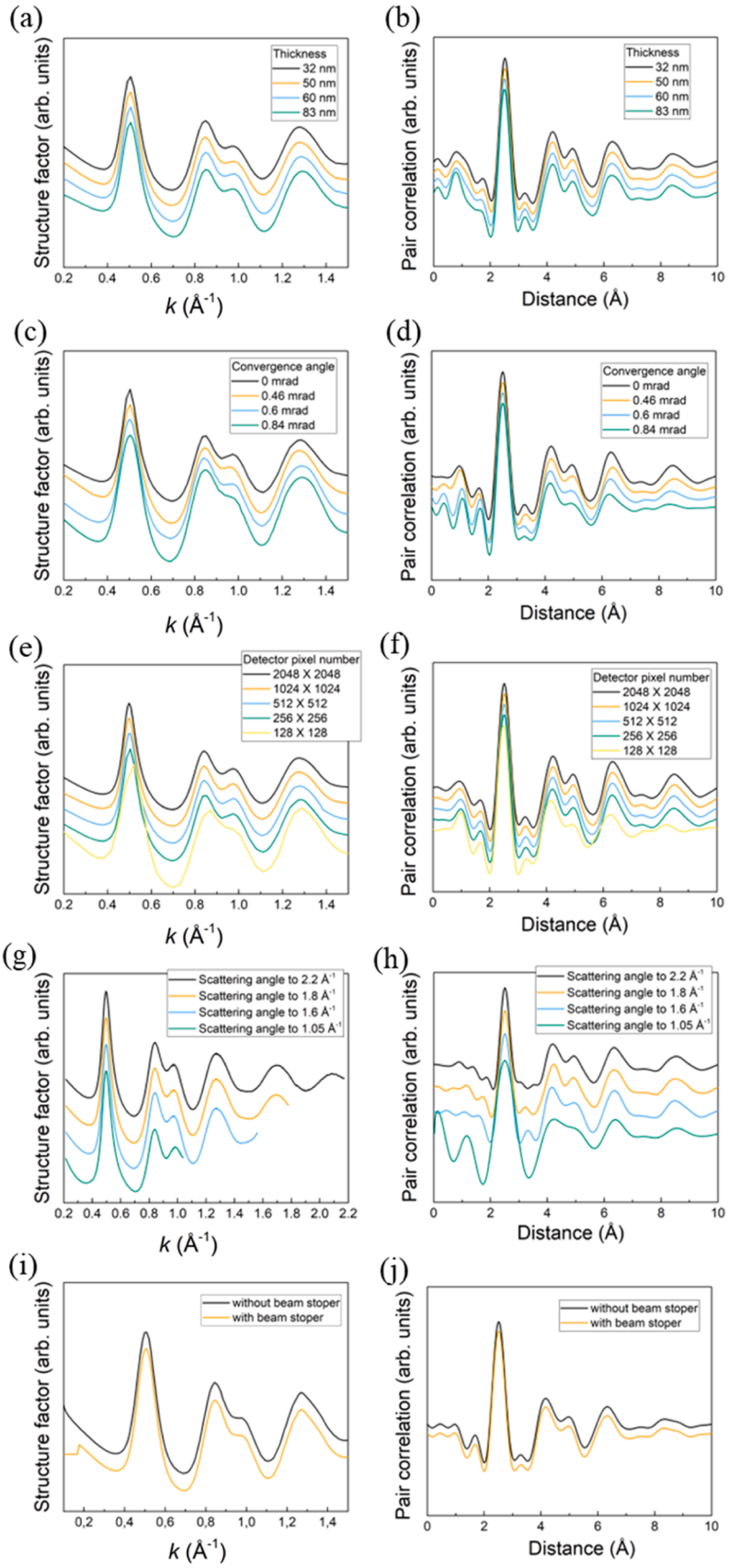

(caption on next page)

Fig. 9. Experimental *S(k)*s and corresponding ePDFs of $Fe_{85.2}Si_{0.5}B_{9.5}P_4Cu_{0.8}$ metallic glass under varying experimental conditions. (a) *S(k)*s obtained from regions of different sample thicknesses: 32 nm, 50 nm, 60 nm, and 83 nm. (b) ePDFs calculated from the *S(k)*s in (a). (c) *S(k)*s collected under four convergence semi-angles: nominally SAED, 0.46 mrad, 0.60 mrad, and 0.84 mrad. (d) ePDFs calculated from the *S(k)*s in (c). (e) *S(k)*s derived from diffraction data rebinned to pixel numbers of 2048×2048, 1024×1024, 512×512, 256×256, and 128×128. (f) ePDFs corresponding to the *S(k)*s in (e). (g) *S(k)*s with maximum scattering vector truncated at k_{max} = 2.2, 1.8, 1.6, and 1.05 Å^{-1}. (h) ePDFs calculated from the *S(k)*s in (g). (i) *S(k)*s processed with two different low-*k* windowing onsets. (j) ePDFs calculated from the *S(k)*s in (i). All *S(k)*s are normalized to their first peak and vertically offset for clarity.

any of the three FOMs.

3.7. Comparison of ground truth PDF with multi-slice simulated ePDF, and experimental ePDF

With optimized simulation parameters and data correction procedures in place, the accuracy of the ePDF was evaluated by direct comparison of three sources: (i) the ground-truth PDF computed from the kimematic diffraction pattern, (ii) the ePDF derived from multislice simulated SAEDs, and (iii) the ePDF obtained from experimental SAED measurements of melt-quenched $Pd_{80}Si_{20}$ metallic glass. Fig. 8a presents an experimental SAED pattern from a 50 nanometer-thick lamella of $Pd_{80}Si_{20}$ and a simulated SAED pattern from a 40 nanometer-thick atomic model. The simulated diffraction pattern closely matches the experimental one, reproducing both ring positions and intensity distributions. The ePDFs were extracted from both patterns using identical analysis workflows (Fig. 8b).

The remaining differences primarily reflect structural deviations between the MD model and the real metallic glass. Specifically, the experimental sample undergoes slower cooling, allowing greater atomic relaxation, while the MD model is generated via rapid quenching, potentially preserving higher-energy local configurations. These results demonstrate that, when supported by optimized data acquisition and processing, electron diffraction can provide quantitatively accurate information on the short- and medium-range atomic structure.

3.8. Experimental investigation on Fe-based metallic glasses

To experimentally validate the simulation-derived insights, a comprehensive series of ePDF measurements were performed on $Fe_{85.2}Si_{0.5}B_{9.5}P_4Cu_{0.8}$ metallic glass, systematically varying key experimental parameters. All datasets were processed using a consistent procedure, including normalization, third-order polynomial background correction, and a Fourier transformation window of 0.2 to 1.45 Å^{-1}.

Four distinct regions with EELS estimated thicknesses of approximately 32 nm, 50 nm, 60 nm, and 83 nm were selected for NBED data acquisition. The corresponding *S(k)*s, obtained after polynomial background subtraction and normalized to their first peak intensities, are shown in Fig. 9a. For clarity, the curves are vertically offset to facilitate the comparison of peak positions. The corrected *S(k)* profiles exhibit consistent oscillatory features and peak positions across all thicknesses. The associated ePDFs, presented in Fig. 9b, display identical atomic correlation features across the examined thickness range. These experimental results align closely with the above simulation outcomes, confirming that accurate ePDFs can still be extracted from thick samples, provided that proper background correction is applied.

The convergence semi-angle was varied across four settings: nominally parallel-beam illumination (SAED mode, α ≈ 0 mrad), and STEM conditions with α = 0.46 mrad, 0.60 mrad, and 0.84 mrad. These values were achieved by adjusting the condenser aperture and beam-forming optics. Fig. 9c presents the corresponding *S(k)* data. Increasing α progressively diminished the visibility of fine structural modulations in *S(k)*, particularly the second peak shoulder at 0.95 Å^{-1}. The resulting PDFs (Fig. 9d) reflect this trend: broader peaks and reduced contrast at large distances were observed at higher convergence angles. Specifically, at α = 0.84 mrad, peak intensities were significantly damped at high distances, and the second coordination shell became poorly resolved. The α = 0.60 mrad condition preserved most structural features and represented a practical trade-off between probe localization and resolution. The SAED (α ≈ 0) data yielded the sharpest ePDFs, reaffirming that low convergence angles, preferably <0.6 mrad, are optimal for NBED-based ePDF acquisition. These observations are consistent with simulation results shown in Fig. 4b

High-resolution diffraction data (2048×2048 pixels, acquired with a Gatan OneView camera) were digitally rebinned to emulate lower-resolution detector conditions: 1024×1024, 512×512, 256×256, and 128×128. All data originated from the same region (70 nm thick) under identical probe conditions (α = 0.6 mrad). The resulting *S(k)*s for each binning level are shown in Fig. 9e. No significant differences were observed among the 2048, 1024, 512, and 256 pixel numbers; the oscillatory features in *S(k)*, including those within the second coordination shell, were well preserved. In contrast, the 128×128 data exhibited marked degradation, with smeared features and reduced contrast in *S(k)* due to low pixel resolution. These distortions were more clearly reflected in the corresponding ePDFs (Fig. 9f). While the ePDFs obtained from 256×256 and higher resolutions retained well-defined peak positions and shapes, the 128×128 condition resulted in broadened peaks, diminished sub-peak resolution, and visible shifts in interatomic distances. In particular, the secondary features within the second coordination shell became less distinct and significantly reduced in intensity. These experimental results corroborate simulation findings (Fig. 5d), confirming that a minimum sampling resolution of 256×256 pixels is required for this Fe-based glass to preserve ePDF fidelity under the measurement conditions used here. Further increases in resolution (512 or 1024 pixels) yielded only marginal improvements, indicating that 256×256 provides a practical lower limit for reliable ePDF extraction up to ~10 Å in real-space resolution.

Fig. 9*g* and h illustrate the effect of k_{max} on the ePDF quality. The experimental SAED pattern is artificially truncated to define various k_{max} values. *S(k)*s obtained from diffraction patterns with k_{max} values of 2.2 Å^{-1}, 1.8 Å^{-1}, 1.6 Å^{-1}, and 1.05 Å^{-1}. The ePDFs were calculated from each corresponding *S(k)*s. The first peak of each ePDF is identical, indicating that the nearest atomic distance is not significantly influenced by the limited k_{max} value. However, the next peaks in the ePDF are partially convoluted at a k_{max} of 1.6 Å^{-1}, with the peak separation becoming notably reduced at 1.05 Å^{-1}. Considering the simulation results shown in Fig. 4a and b, the ePDF analysis of real metallic glass shows similar results. Capturing the third diffraction ring of an amorphous diffraction pattern ensures reliable ePDF analysis and is considered an optimal balance between resolution and experimental feasibility.

In the experimental case, where the illuminated atoms and orientation sampling of constituent clusters were substantially higher than in the simulation conditions, the high-angle scattering intensity exhibited a sufficiently good smoothing to enable reliable ePDF calculations. Under these conditions, extending k_{max} beyond the third diffuse ring resulted in only marginal improvements in the ePDF, primarily preserving rather than enhancing its quality. The effect of low-*k* windowing was also evaluated experimentally using onset values between approximately 0.1 Å^{-1} and 0.2 Å^{-1}. As long as the onset remained below the first minimum of *S(k)* and excluded the central beam tail, the resulting ePDFs showed no significant change, in agreement with the simulations in Fig. 4d

4. Conclusions

In this study, a comprehensive investigation was conducted to elucidate the effects of key experimental parameters on the accuracy and fidelity of ePDF analysis. Through a combination of detailed multi-slice simulations and targeted experimental validation on $Pd_{80}Si_{20}$ and $Fe_{85.2}Si_{0.5}B_{9.5}P_4Cu_{0.8}$ glasses, the following conclusions and practical recommendations were established for optimizing ePDF measurements:

- Sample thickness and multiple scattering

Sample thickness significantly impacts ePDF fidelity due to increased multiple elastic scattering. This introduces low-frequency background deviations and causes slight peak shifts toward higher scattering angles, leading to underestimated interatomic distances. Simulations based on the $Pd_{80}Si_{20}$ model show that peak intensity and sharpness degrade with increasing thickness, with peak position shifts up to ~1.2 % from 20 nm to 100 nm. Multiple scattering can also produce spurious peaks at integer multiples (e.g., 2×, 3×) of real interatomic distances, complicating structural interpretation. While low-order polynomial background correction (typically < 4th order) helps suppress low-frequency background artifacts, it does not fully eliminate multiple scattering effects. To address this, a rigorous analytical deconvolution based on a 2D self-convolution model was employed, which effectively restores peak positions and reduces intensity artifacts. When followed by low-order polynomial background correction, this approach yields high-fidelity ePDFs with consistent structural information across a wide range of sample thicknesses.

- Beam convergence semi-angle and detector pixel number

The accuracy of ePDF analysis is strongly influenced by both the electron beam convergence angle and the angular sampling of the diffraction pattern. Our results show that convergence angles larger than ~0.6 mrad degrade structural resolution due to angular blurring and frequency-dependent damping in the *S(k)*. Similarly, insufficient detector pixel resolution (below 256×256) leads to aliasing artifacts and loss of real-space structural detail. For reliable ePDF interpretation, small convergence angles and adequate angular sampling are essential to preserve both short- and medium-range order.

- Maximum and minimum scattering angle

The accuracy of ePDF reconstruction is sensitive to both the k_{max} and the treatment of the central beam (k_{onset}). A sufficiently large k_{max} (greater than or equal to 1.3 $Å^{-1}$) is essential to capture medium-range structural features and avoid Fourier truncation artifacts. Disordered materials like metallic glasses are less sensitive to high-*k* truncation but still benefit from extended *k*-range for improved resolution. At low *k*, improper handling of the central beam, either including too much of the direct beam tail or masking too much low-*k* data, can introduce baseline distortions and peak artifacts. A balanced choice, avoiding the center beam tail and before the 1st minimum of *S(k)*, yields reliable and artifact-minimized ePDFs. These results highlight the importance of selecting reciprocal-space windows for accurate ePDF analysis.

- Effect of noise and electron beam precession

Electron dose plays a critical role in determining the signal-to-noise ratio. At low doses, increased noise leads to distortions in the ePDF beyond the first coordination shell. Higher doses yield cleaner *S(k)*s and more accurate ePDFs, while short-range information is relatively robust at low dose conditions. For sensitive materials, careful dose optimization or noise-reduction strategies are necessary for reliable analysis. Electron beam precession enhances ePDF quality by averaging out the orientation effects of local structurally constituent clusters when NBED is used. Simulations with 0, 1, and 3-degree precession angles show that precession smooths the *S(k)* and clarifies medium-range features in the ePDF, while preserving short-range peaks. This confirms that moderate precession improves interpretability, particularly for weak or diffuse signals, for NBED experiments.

Overall, this study establishes a concrete framework for designing and interpreting ePDF experiments. The guidelines provided herein are broadly applicable to investigations of amorphous, nanostructured, or heterogeneous materials, and will facilitate more precise probing of short- and medium-range atomic order in materials science.

Data availability

The data generated in this study are available at KITOpen through the following DOI: https://doi.org/10.35097/cbx4u9fhfzpdpwds.

CRediT authorship contribution statement

Sangjun Kang: Writing – review & editing, Writing – original draft, Visualization, Validation, Supervision, Software, Resources, Project administration, Methodology, Investigation, Funding acquisition, Formal analysis, Data curation, Conceptualization. **Hyeyoung Cho:** Writing – review & editing, Writing – original draft, Visualization, Validation, Methodology, Investigation. **Maximilian Töllner:** Writing – review & editing, Writing – original draft, Validation, Methodology, Investigation. **Vanessa Wollersen:** Writing – review & editing, Writing – original draft, Resources, Methodology, Investigation, Formal analysis. **Di Wang:** Writing – review & editing, Writing – original draft, Validation, Methodology, Investigation. **Hionsuck Baik:** Writing – review & editing, Writing – original draft, Methodology, Investigation, Conceptualization. **Marie Joëlle Perera:** Writing – review & editing, Writing – original draft, Validation, Resources, Methodology. **Omar Adjaoud:** Writing – review & editing, Writing – original draft, Validation, Methodology, Investigation, Data curation. **Karsten Albe:** Writing – review & editing, Writing – original draft, Validation, Methodology, Investigation, Conceptualization. **Christian Kübel:** Writing – review & editing, Writing – original draft, Visualization, Validation, Supervision, Resources, Project administration, Funding acquisition, Conceptualization. **Xiaoke Mu:** Writing – review & editing, Writing – original draft, Visualization, Validation, Supervision, Methodology, Investigation, Funding acquisition, Data curation, Conceptualization.

Declaration of competing interest

The authors declare that they have no known competing financial interests or personal relationships that could have appeared to influence the work reported in this paper.

Acknowledgments

The authors express their gratitude to the Karlsruhe Nano Micro Facility (KNMFi) for their assistance and for providing access to FIB and TEM facilities. X. M. acknowledges the financial support from the Fundamental Research Funds for the Central Universities (grant number lzujbky-2025-ytA02). S.K. and C.K. acknowledge the support from collaborative research centre FLAIR (Fermi level engineering applied to oxide electroceramics), which is funded by the German Research Foundation (DFG), project-ID 463184206 – SFB 1548. This work was supported by the Technology Innovation Program (RS-2024–00418991) funded By the Ministry of Trade, Industry & Energy (MOTIE, Korea). S. K. expresses sincere gratitude to Dr. Yongsoo Yang and Dr. Juhyeok Lee for their insightful discussion. Additionally, the authors appreciate the support received from the Joint Lab Model Driven Materials Characterization (MDMC) and acknowledge backing from the Helmholtz Imaging Project (HIP) BRLEMM.

Supplementary materials

Supplementary material associated with this article can be found, in the online version, at doi:10.1016/j.ultramic.2025.114295.

References

[1] V. Petkov, Pair distribution functions analysis, Charact. Mater. 1361 (2012).
[2] T. Proffen, S. Billinge, T. Egami, D. Louca, Structural analysis of complex materials using the atomic pair distribution function—a practical guide, Z. Krist.-Cryst. Mater. 218 (2003) 132–143.
[3] M.W. Terban, S.J. Billinge, Structural analysis of molecular materials using the pair distribution function, Chem. Rev. 122 (2021) 1208–1272.
[4] S.J. Billinge, M. Thorpe, Local Structure from Diffraction, Springer Science & Business Media, 2006.
[5] B. Warren, X-ray diffraction of vitreous silica, Z. Krist.-Cryst. Mater. 86 (1933) 349–358.
[6] H.E. Fischer, A.C. Barnes, P.S. Salmon, Neutron and x-ray diffraction studies of liquids and glasses, Rep. Prog. Phys. 69 (2005) 233.
[7] C. Benmore, A review of high-energy X-ray diffraction from glasses and liquids, Int. Sch. Res. Not. 2012 (2012) 852905.
[8] P. Egelstaff, An Introduction to the Liquid State, Elsevier, 2012.
[9] T. Egami, Structural relaxation in amorphous Fe40Ni40P14 B6 studied by energy dispersive X-ray diffraction, J. Mater. Sci. 13 (1978) 2587–2599.
[10] Y. Suzuki, J. Haimovich, T. Egami, Bond-orientational anisotropy in metallic glasses observed by x-ray diffraction, Phys. Rev. B 35 (1987) 2162.
[11] B. Warren, X-ray Diffraction, Dover, 1990.
[12] J.B. Souza Junior, G.R. Schleder, J. Bettini, I.C. Nogueira, A. Fazzio, E.R. Leite, Pair distribution function obtained from electron diffraction: an advanced real-space structural characterization tool, Matter 4 (2021) 441–460.
[13] J.L. Labar, K. Hajagos-Nagy, P.P. Das, A. Gomez-Perez, G. Radnoczi, Simple ePDF: a pair distribution function method based on electron diffraction patterns to reveal the local structure of amorphous and nanocrystalline materials, Nanomater. (Basel) 13 (2023).
[14] T.E. Gorelik, R. Neder, M.W. Terban, Z. Lee, X. Mu, C. Jung, T. Jacob, U. Kaiser, Towards quantitative treatment of electron pair distribution function, Acta Crystallogr. B Struct. Sci. Cryst. Eng. Mater. 75 (2019) 532–549.
[15] J.B.S. Junior, G.R. Schleder, J. Bettini, I.C. Nogueira, A. Fazzio, E.R. Leite, Pair distribution function obtained from electron diffraction: an advanced real-space structural characterization tool, Matter 4 (2021) 441–460.
[16] C. Ophus, Four-dimensional scanning transmission electron microscopy (4D-STEM): from scanning nanodiffraction to ptychography and beyond, Microsc. Microanal. 25 (2019) 563–582.
[17] P.M. Voyles, J.R. Abelson, Medium-range order in amorphous silicon measured by fluctuation electron microscopy, Sol. Energy Mater. Sol. Cells 78 (2003) 85–113.
[18] P. Zhang, J.J. Maldonis, Z. Liu, J. Schroers, P.M. Voyles, Spatially heterogeneous dynamics in a metallic glass forming liquid imaged by electron correlation microscopy, Nat. Commun. 9 (2018) 1–7.
[19] S. Huang, C. Francis, J. Ketkaew, J. Schroers, P.M. Voyles, Correlation symmetry analysis of electron nanodiffraction from amorphous materials, Ultramicroscopy 232 (2022) 113405.
[20] S. Kang, X. Mu, M. Töllner, D. Wang, C. Minnert, K. Durst, A. Caron, R. Dunin-Borkowski, J. McCord, C. Kübel, Large-angle Lorentz 4D-STEM for simultaneous magnetic and atomic structure mapping, (2024).
[21] S. Kang, D. Wang, A. Caron, C. Minnert, K. Durst, C. Kubel, X. Mu, Direct observation of quadrupolar strain fields forming a shear band in metallic glasses, Adv. Mater. 35 (2023) e2212086.
[22] S. Kang, D. Wang, C. Kübel, X. Mu, Importance of TEM sample thickness for measuring strain fields, Ultramicroscopy 255 (2024) 113844.
[23] S. Kang, V. Wollersen, C. Minnert, K. Durst, H.-S. Kim, C. Kübel, X. Mu, Mapping local atomic structure of metallic glasses using machine learning aided 4D-STEM, Acta Mater. 263 (2024) 119495.
[24] X. Mu, L. Chen, R. Mikut, H. Hahn, C. Kübel, Unveiling local atomic bonding and packing of amorphous nanophases via independent component analysis facilitated pair distribution function, Acta Mater. 212 (2021).
[25] X. Mu, A. Mazilkin, C. Sprau, A. Colsmann, C. Kübel, Mapping structure and morphology of amorphous organic thin films by 4D-STEM pair distribution function analysis, Microscopy 68 (2019) 301–309.
[26] X. Mu, D. Wang, T. Feng, C. Kübel, Radial distribution function imaging by STEM diffraction: phase mapping and analysis of heterogeneous nanostructured glasses, Ultramicroscopy 168 (2016) 1–6.
[27] S. Billinge, Local structure from total scattering and atomic pair distribution function (PDF) analysis, (2008).
[28] J. Pendry, Multiple scattering theory of electron diffraction, Surf. Sci. 299 (1994) 375–390.
[29] G. Anstis, Z. Liu, M. Lake, Investigation of amorphous materials by electron diffraction—the effects of multiple scattering, Ultramicroscopy 26 (1988) 65–69.
[30] S. Plimpton, Fast parallel algorithms for short-range molecular dynamics, J. Comput. Phys. 117 (1995) 1–19.
[31] J. Ding, Y.-Q. Cheng, H. Sheng, E. Ma, Short-range structural signature of excess specific heat and fragility of metallic-glass-forming supercooled liquids, Phys. Rev. B—Condens. Matter Mater. Phys. 85 (2012) 060201.
[32] Y. Cheng, J. Ding, E. Ma, Local topology vs. atomic-level stresses as a measure of disorder: correlating structural indicators for metallic glasses, Mater. Res. Lett. 1 (2013) 3–12.
[33] D.Z. Chen, Q. An, W.A. Goddard III, J.R. Greer, Ordering and dimensional crossovers in metallic glasses and liquids, Phys. Rev. B 95 (2017) 024103.
[34] Y. Hu, F. Li, M. Li, H. Bai, W. Wang, Five-fold symmetry as indicator of dynamic arrest in metallic glass-forming liquids, Nat. Commun. 6 (2015) 8310.
[35] J. Madsen, T. Susi, abTEM: ab initio transmission electron microscopy image simulation, Microsc. Microanal. 26 (2020) 448–450.
[36] I. Lobato, D. Van Dyck, An accurate parameterization for scattering factors, electron densities and electrostatic potentials for neutral atoms that obey all physical constraints, Found. Crystallogr. 70 (2014) 636–649.
[37] P. Debye, Light scattering in solutions, J. Appl. Phys. 15 (1944) 338–342.
[38] P. Debye, Molecular-weight determination by light scattering, J. Phys. Chem. 51 (1947) 18–32.
[39] A. Weickenmeier, H. Kohl, Computation of absorptive form factors for high-energy electron diffraction, Found. Crystallogr. 47 (1991) 590–597.
[40] E.J. Kirkland, Advanced Computing in Electron Microscopy, Springer, 1998.
[41] J. Ankele, J. Mayer, P. Lamparter, S. Steeb, Quantitative electron diffraction data of amorphous materials, Z. Naturforsch. A 60 (2005) 459–468.
[42] Z. Yang, L. Tang, T. Wen, K.-M. Ho, C.-Z. Wang, Effects of Si solute on the glass formation and atomic structure of Pd liquid, J. Phys. 31 (2019) 135701.
[43] D.A. Keen, Total scattering and the pair distribution function in crystallography, Crystallogr. Rev. 26 (2020) 143–201.
[44] P.A. Midgley, A.S. Eggeman, Precession electron diffraction–a topical review, IUCrJ 2 (2015) 126–136.